

## Article

# Modelling and Simulation of Quasi-Resonant Inverter for Induction Heating under Variable Load

Enrico Spateri, Fredy Ruiz  and Giambattista Grusso \* 

Dipartimento di Elettronica Informazione e Bioingegneria, Politecnico di Milano, Piazza Leonardo da Vinci 32, 20133 Milano, Italy

\* Correspondence: giambattista.grusso@polimi.it

**Abstract:** Single-switch quasi-resonant DC inverters are preferred in low-power induction-heating applications for their cheapness. However, they pose difficulties in enforcing soft-switching and show limited controllability. A good design of these converters must proceed in parallel with the characterization of the load and the operating conditions. The control of the switching frequency has a critical relationship to the non-linear behavior of the load due to electro-thermal coupling and geometrical anisotropies. Finite element methods enable the analysis of this kind of multiphysics coupled systems, but the simulation of transient dynamics is computationally expensive. The goal of this article is to propose a time-domain simulation strategy to analyze the behavior of induction heating systems with a quasi-resonant single-ended DC inverter using pulse frequency modulation and variable load. The load behavior is estimated through frequency stationary analysis and integrated into the time-domain simulations as a non-linear equivalent impedance parametrized by look-up tables. The model considers variations in temperature dynamics, the presence of work-piece anisotropies, and current harmonic waveforms. The power regulation strategy based on the control of the switch turn-on time is tested in a case study with varying load and it is shown that it is able to maintain the converter in the safe operation region, handling variations up to of 22% in the equivalent load resistance.

**Keywords:** electrical converters; induction heating; electro-thermal system; multiphysics modelling; circuitual equivalent



**Citation:** Spateri, E.; Ruiz, F.; Giambattista, G. Modelling and Simulation of Quasi-Resonant Inverter for Induction Heating under Variable Load. *Electronics* **2023**, *12*, 753. <https://doi.org/10.3390/electronics12030753>

Academic Editor:  
Minh-Khai Nguyen

Received: 23 November 2022

Revised: 18 January 2023

Accepted: 25 January 2023

Published: 2 February 2023



**Copyright:** © 2023 by the authors. Licensee MDPI, Basel, Switzerland. This article is an open access article distributed under the terms and conditions of the Creative Commons Attribution (CC BY) license (<https://creativecommons.org/licenses/by/4.0/>).

## 1. Introduction

Induction heating (IH) technology is not only substituting conventional heating systems such as home cookers, but it is an alternative in those systems in which heating of a workpiece is not the final goal [1,2]. It is considered in many domestic systems or small industrial applications where the heating of an accessory or a tool is necessary for other purposes. The requirement to obtain a high profit from those final products orients the choice for a low-cost IH system.

Authors in [3] give an overview of the main converter topologies for IH, highlighting that the hardware selection for variable frequency operation is one of the main challenges in the converter design, while energy efficiency is one of the main performance indicators of any converter, as stated in [4]. Novel converters, supplied by renewable sources [5], with novel modulation techniques [6] and with strategic switching delays [7] have been recently proposed to augment efficiency and robustness. Ref. [8] proposes a full-bridge inverter for IH with high efficiency and improved power regulation. However, [9] shows that the cheapest converter for medium–high frequency and low-power IH applications is the quasi-resonant single-switch DC inverter. However, while in more complex resonant inverters, the current in the resonant tank is managed by the control strategy of two or more switches, allowing an efficient control in the desired frequency range, in a single-switch inverter the design of the converter has to be tightly coupled with the analysis of

the coil-workpiece system. Finally, some direct online load identification techniques have been developed to evaluate the load in real induction heating systems with full-bridge or half-bridge inverters [10,11]. Still, these methods require to process current measurements in real time, augmenting the complexity of the systems.

Single-switch inverters must be specifically designed for each single application because their main drawback is their scarce flexibility, as shown in [12,13]. Due to the single switch and its lack of control inputs, it has a quite narrow control window. Moreover, controlling the switching frequency has a very critical relationship with the load behavior. The coupled analysis of the load with the design of the converter parameters is necessary to estimate the IH process behavior and manage the soft-switching. Additionally, information about the safe operative area and the working region must be predicted during the product development.

Finite element analysis (FEA) methods are the most complete tools for the analysis and optimization of multiphysics problems [14,15], such as the design of power inverters for IH solutions [16,17]. Nevertheless, they have some limitations for the analysis of transient domains for a coupled systems with physics with very different time resolutions [18]. Moreover, the simulation of the control scheme of one of these physics results in high computational and time costs. Usually, stationary frequency analysis is taken into account for the system described in the nominal working frequency and current state. However, the electro-thermal transient dynamics and variations in coil-workpiece geometry are not considered, see, e.g., [19]. Even though FEA cannot be used directly for the analysis of load-converter control, some informative results can be extracted to represent the load considering non-linear phenomena. Indeed, non-linear electro-thermal and magneto-thermal properties and workpiece anisotropies can have a non-negligible impact on the converter's performance and its regulation during the heating process [20].

The goal of this article is to develop a simulation tool for an IH system with a quasi-resonant single-ended DC inverter and pulse frequency modulation (PFM) control, for the analysis of the regulatory scheme and electrical operative limits with varying load during the design phase of the system (Figure 1). In this paper, we propose to use a simulation-based methodology for load identification, helpful for the design and simulation of the inverter system. The equivalent model parameters of the load are indirectly represented as look-up tables in order to emulate the load as an equivalent circuitual element in the integrated load-converter system, similar to the method used in [21]. The lumped parameters are extracted and identified from FEA simulations considering the dependencies of the electromagnetic coupling with the temperature dynamics, the presence of anisotropies, the prescribed current amplitude and frequency.

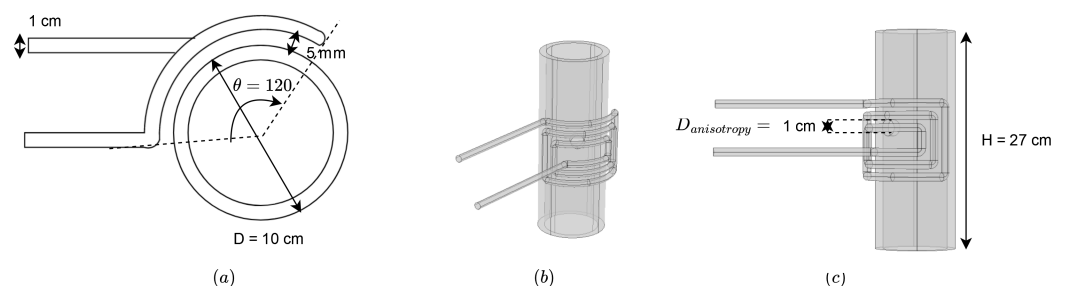


**Figure 1.** 3D geometry analyzed with FEM: XY-section as upper view (a), side view (b,c) and timelapse of an anisotropy sliding.

The effects of these variations on the converter are analyzed on different time scales: a period of the resonant tank, a period of the power grid source, and the entire heating horizon. The integration of time variant parameters allows the tracking of the behavior of the load during the heating process. The results of a simulation integrating the power control strategy during the complete heating process with non-linear equivalent parameters are described and analyzed from the point of view of the converter performance.

The article is structured as follows: the design problem, similar to the one described in [22], is described in Section 1. Then, the converter and the safe operating areas are briefly analyzed in Section 2. In Section 3, the methodology for the extraction and integration of variable parameters as an equivalent circuit is discussed. The results of this methodology are discussed in Section 4: the variations of the load concerning external conditions and inverter quantities are discussed through the freewheeling analysis of the resonant tank. Finally, The results for different operative needs with workpiece anisotropies are analyzed for three different time scales.

## 2. Problem Description

The setup considers the heating of a moving tube as an element of a more complex maintenance system tool, for the homogeneous heating of axi-symmetrical workpieces. In this case study, the workpiece has some joints on its sides, then the coil can not wrap up the tube due to the geometrical constraints. A pure copper curved pancake coil is designed to heat up only an angular section of  $120^\circ$  of the moving tube along its symmetry axis (z-axis). Figure 1a represents the geometry of the case study. Due to its asymmetry, it is difficult to describe the induction-heating problem analytically. Moreover, for the converter design, it is necessary to define the load response to the inverter supply for different operative situations as temperature variations or the presence of anisotropies in the heated material. In Figure 1b,c, an anisotropy is represented as a hole passing in the heated area during the pipe sliding. The geometrical parameters are listed in Table 1. A scheme of the complete converter plus heated piece geometry is shown in Figure 2. A filter and a rectifier bridge for the AC–DC conversion supplies a single ended DC quasi resonant converter with parallel RL-C resonant tank. The aim is to represent the coil and the electromagnetic coupling with the workpiece as a series equivalent RL variable circuit, estimated through frequency stationary FEA simulations. The resulting model is exploited to:

- Test the inverter for different resonant capacitor values in order to manage the working region;
- Assess the control strategy validity in different operative situations;
- Track the load behavior during the heating process.

**Table 1.** Geometrical parameters for the coil, the pipe, and the anisotropy.

Parameter	Measure	Parameter	Measure
Outer radius	5 cm	Height	27 cm
Inner radius	4 cm	Anisotropy radius	1 cm
Coil distance	5 mm	Coil length	125 cm
Windings number	10	Coil radius	5 cm

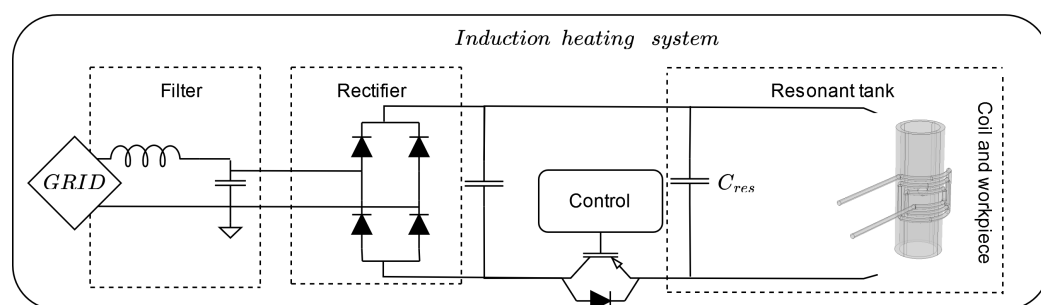


**Figure 2.** IH system with single ended DC quasi-resonant converter.

## 3. The Quasi-Resonant Single Switch Inverter

In this section, the working principle of the single-ended quasi-resonant inverter is shortly described in its phases and its safe operating limitations to identify the main param-

eters involved in its working principle. As shown in Figure 3, the inverter is composed of a parallel RL-C resonant tank which represents the coil plus workpiece coupling, connected in parallel to a resonant capacitor. The tank is supplied by a DC-voltage source and controlled by an IGBT with a freewheeling diode. The converter works in three time phases:

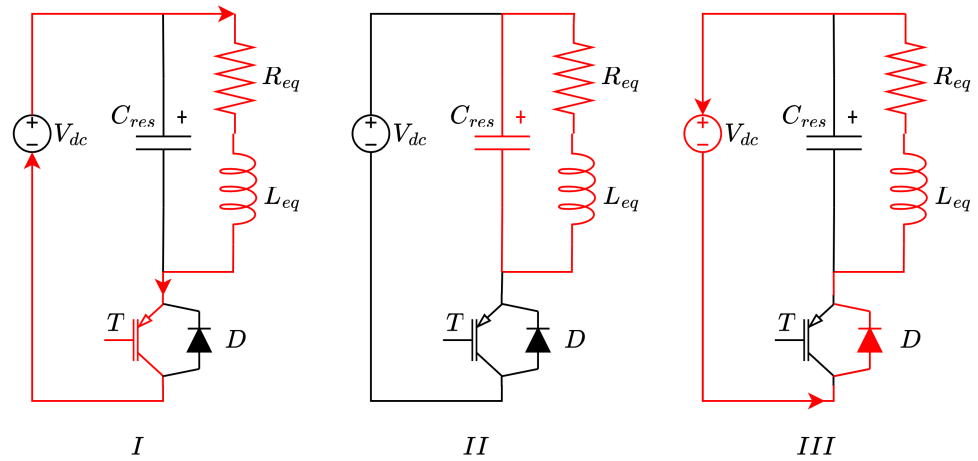


Figure 3. Quasi-resonant converter and three stages of working.

3.1. First Phase

In the first phase, the IGBT is closed, and the current passes through the RLC circuit. The capacitor is suddenly charged to the source voltage, while the current passes through the inductor. By balancing the voltage in the red loop in Figure 3I, considering an ideal switch, we get:

$$V_{dc}(t) = R_{eq}I_{RL} + L_{eq}\dot{I} \tag{1}$$

The current in the inductor is defined by:

$$I_{RL}(t) = \frac{V_{dc}}{L_{eq}}(1 - e^{-\frac{R_{eq}}{L_{eq}}t}) \tag{2}$$

If the switching period is shorter than the circuit time constant  $\frac{L_{eq}}{R_{eq}}$ , and the achieved peak current is low, the current time derivative is the ratio  $\frac{V_{DC}}{L_{eq}}$ .

3.2. Second Phase

The IGBT is opened while the current flows in the inductor. The current discharges the capacitor and the voltage on the IGBT collector increases. The current behavior depends on the resonant tank frequency according to:

$$I_{RL}(t) = Ae^{-\alpha t}\cos(\omega t) + Be^{-\alpha t}\sin(\omega t) = A_0e^{-\alpha t}\cos(\omega t - \phi) \tag{3}$$

where the decay rate is  $\alpha = \frac{R_{eq}}{L_{eq}}$  and the resonant tank frequency is  $\omega = \sqrt{\frac{1}{L_{eq}C_{res}} - \frac{R_{eq}^2}{4L_{eq}^2}}$ .

The parameters can be calculated by solving the differential equation system with  $V_{DC}$  as the initial voltage on the capacitor [9].

3.3. Third Phase

The IGBT remains open, and the current flows backward from the diode and the coil. The behavior of the current has the same form of Equation (2).

### 3.4. No Load

If the load is absent, the equivalent inductance increases and there is a resistance drop. Thus, the resonant tank's freewheeling can be used to detect the workpiece in a detection strategy. In the detection operating mode, the IGBT is controlled by a simple step signal or a square wave signal with low-frequency switching for repetitive workpiece detection events. When the IGBT is closed, the voltage across the capacitor is the supply voltage. When the IGBT is opened, the freewheeling of the RLC resonant tank is measured, and the exponential decay reveals the coil-workpiece equivalent decay ratio  $\alpha$ .

### 3.5. The Safe Operating Region

The semiconductor components are usually stressed during the switching at high frequencies. The safe operating region primarily consists in the analysis of the voltage, current and temperature behavior during the converter operation. The main capacitor constraint is the maximum AC voltage, while the IGBTs impose more limitations. The first IGBTs constraint is given by the maximum average losses. These losses are strictly dependent on the RMS current passing in the IGBT:

$$P_{IGBT} = R_{IGBT}(T)I_{IGBT}^2 \quad (4)$$

where  $R_{IGBT}(T)$  is the temperature dependent IGBT resistance. Another limitation regards the maximum rated voltage which affects the freewheeling diode. If the voltage reaches the breakdown value, the diode conducts currents during the current fall down and the resonance in the RLC circuit is lost.

Starting from the Equation (3) and the current time derivative, the maximum capacitor voltage is dependent from the maximum fall down slope during the second phase of the resonant cycle.

$$|V_{C_{res}}|_{max} = R_{eq}I_{RL} + L_{eq}\dot{I}_{RL} \quad (5)$$

Using a pure harmonic approximation, the maximum slope of the current occurs when  $I_{RL}$  is zero at  $t = \frac{1}{4\hat{f}}$ , where  $\hat{f}$  is the estimated resonant frequency. The resistive term of Equation (5) is neglected for simplicity. Thus, assuming an harmonic approximation and linear slope during the  $I_{RL}$  current rise-up, this constraint is modeled as:

$$|V_{dc}| + \left| \frac{L(\alpha + \omega)I_{max}}{\sqrt{2}} e^{-\frac{\alpha}{4\hat{f}}} \right| < V_{C,max} \quad (6)$$

Finally, the IGBTs turn-on time must be considered for the definition of the frequency range. The turn-on time is related to the features of the resonant load. If the collector voltage is not null when the IGBT is turned on, a high-peak current flows from the capacitor to the IGBT. Even if its power loss is low, it can stress the semiconductors. Ideally, during the switching lapse the supplied DC voltage must be equal to the voltage drop on the inductor. The existence of a zero collector voltage point can be determined by solving the Equation (7) for  $\phi \in (0, 2\pi)$ :

$$V_{dc} = -L\omega I_{max} e^{-\frac{\alpha\phi}{\omega}} \sin(\phi) \quad (7)$$

which comes from Equation (5) in the transition between the third and the first phase.

All the RL-C components of the resonant tank and its frequency affect the inverter operation and its safe operative region. In order to select a good resonant capacitor and to define an adequate closed-loop power-regulation strategy, it is required to simulate the inverter for different conditions, verifying that all the constrained variables are below their

safe operative limit thresholds. Then, a strategy to emulate the load equivalent parameters is proposed in the following section.

#### 4. Load Emulation Methodology

An accurate representation of the coil-workpiece equivalent circuit under different working conditions is not trivial due to the non-linearities of the coupling phenomena. Moreover, the main problem during the design of the converter and the evaluation of the safe operative area concerns the converter response to the variable equivalent load parameters.

The non-linear phenomena affecting the coil-workpiece behavior can be classified as electro-magnetic, electro-thermal, magneto-thermal, motion, and boundary effects [23]. These non-linearities affect directly or indirectly the different parts of the IH system:

- The electro-magnetic non-linearities in the coil are represented mainly by the mutual effects between the induced field, the current and the wire AC resistance. The effect is different in the workpiece ferromagnetic materials: the eddy currents circulating in the workpiece are enhanced by a non-linear relation between the induction field and the magnetic field. The equivalent RL values change with the current waveform amplitude and frequency:
  1. The current amplitude changes the equivalent impedance values according to the effective working point on the BH saturation curve of the workpiece. For small signals, the magnetic permeability is fixed and the problem is considered linear. For high currents, the slope of the BH curve decreases, and the effective inductance reduces to the one without the workpiece;
  2. For higher frequencies, the current has a higher slope and thus, according to the Faraday law, higher eddy currents flow inside the material. Then, the equivalent resistance seen by the converter increases, representing the rise of the dissipated power for the same current amplitude in the RL branch.
- Any geometrical variation of the workpiece morphology or the relative position is called anisotropy. Due to these volume defects and variations, the total eddy current inside the material change drastically. For missing ferromagnetic volumes, the inductance reduces to the one without the workpiece. However, it raises when the workpiece changes the magnetic field curled path (as pancake coils), and decreases when the material does not affect its path (workpiece inside a solenoidal coil). Moreover, when the anisotropy cuts the workpiece, the flux, and the currents concentrate on the borders;
- The temperature influences the material parameters as electro-thermal and magneto-thermal couplings. The variation of the non-linear BH curve during the heating process is represented by the magneto-thermal non-linearities: for higher temperatures the BH curve saturation decreases until it becomes linear at Curie temperature. For small ranges of temperature, the main effect is the linear electro-thermal variation of the electrical resistivity;
- According to the Lorentz formula, the sliding movement generates an additional eddy current due to the time derivative of the induction field. However, for very high frequencies, the velocity in the magnetic field is dominated by the wireless frequency variation in the Faraday law.

In the literature, the coil-workpiece impedance has been represented as an equivalent RL circuit, see, e.g., [18]. However, the variations generated by the current amplitude and frequency are usually neglected. Additionally, the effect of the temperature on the equivalent circuit has not been considered. Thus, an alternative equivalent strategy is proposed now to represent these loads under a large spectrum of operating conditions of the converter, where the equivalent RL circuit is represented as a time variant lumped impedance, parametrized by the current waveform characteristics and the temperature.

#### 4.1. FEM Simulation

Time-dependent electromagnetic FEM analysis is computationally expensive and frequency stationary simulations are usually preferred for their lower request of processing capabilities. Then, a parametrized frequency-stationary FEA of the coil-workpiece system is performed to extract the equivalent average values for the resistance and inductance with respect to all the variant parameters, that in the case of the IH system are the current amplitude and frequency, and the workpiece temperature. In order to use the resulting lumped parameters in time-domain converter simulations we make the assumption that the current waveform is close to harmonic.

#### 4.2. Parameters Extraction

The circuit parameters are extracted from the FEA simulations for each set of operation parameters (prescribed current amplitude and frequency, and workpiece temperature) according to the following equations [24]:

$$L_{eq} = \Re \left[ \int_{V_{coil}} \frac{\vec{A} \cdot \vec{J}_0}{I_{rms}^2} \delta V_{coil} + \int_{V_{mat}} \frac{\vec{A} \cdot \vec{J}_{eddy}}{I_{rms}^2} \delta V_{mat} \right] \quad (8)$$

$$R_{eq} = \frac{P_{generated}}{I_{rms}^2} \quad (9)$$

where  $\vec{A}$  is the magnetic vector potential,  $\vec{J}_0$  is the prescribed current,  $\vec{J}_{eddy}$  is the induced current in the workpiece, which generates a power  $P_{generated}$ . The two integrals are calculated in the volume of the coil  $V_{coil}$  and in the material domain volume  $V_{mat}$ , respectively.

#### 4.3. Look-Up Table Integration

The obtained values of the RL circuit are integrated in the converter simulation to represent the coil-workpiece as a time variant equivalent circuit through a set of two look-up tables. The look-up tables have three decision inputs: the RMS current value, the observed frequency of the current in the RL branch and the temperature predicted by the surrogate thermal model.

An equivalent circuit simulation [25] with varying operative conditions is exploited for the analysis of the coupled converter-load behavior. In Figure 4 it is represented the DC inverter and its integration with the electro-thermal systems. The RMS current value is the average over the resonance period of the tank. The frequency is estimated by a set-reset flip flop and a sample and hold system that measures the time elapsed between two zero current crossings.

The dynamics of the temperature evolution is represented by a surrogate model for the thermal dynamics. An equivalent RC circuit emulates the dynamics of the average surface temperature, given the power dissipated by the equivalent resistance.

The interpolated resistance value is fed to a varying resistance element, while the inductance value is used by a controlled current source that emulates the inductance behavior. The introduction of anisotropies is performed by using parallel look-up tables and customized switching functions.

A PFM control regulates the IGBT turn-on time. The power reference  $P_{ref}$  is compared to the average resistor power calculated over one half of the grid period, and fed to a PI controller that modulates the IGBT turn on time according to the real-time measured frequency. Usually, the turn-on time is about the 35% of the waveform period, the upper and lower limits on the turn-on time are set to 10% and 40% to maintain the harmonic waveform approximation. An outer nested controller can easily reach the temperature regulation.

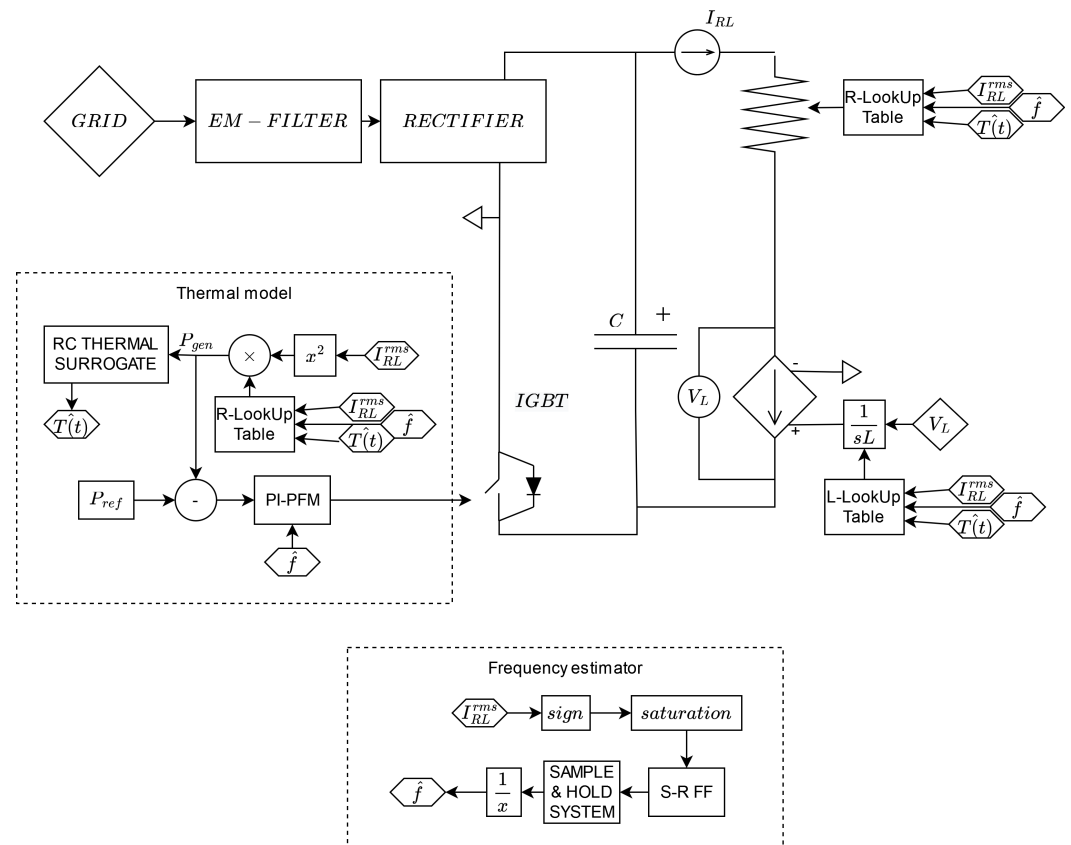


**Figure 4.** Inverter simulation system and PFM control with the thermal model and the integration of the equivalent loads.

### 5. Case Study Results

The methodology is exploited to extract the equivalent resistance and inductance for sweep currents and frequencies (0.1 A to 22.5 A and 80 kHz to 100 kHz).

The resistance and inductance are represented in the Figure 5. The maps highlight the electro-magnetic non-linear behavior. The first observation concerns the equivalent resistance and optimal solution. The efficiency of induction heating systems is based on the ratio between the energy delivered to the workpiece and all the losses including the coil and converter ones. This is equivalent to the ratio between of equivalent resistances, thus high equivalent resistance is preferred. Secondary, the RL parameters are constant for currents under 2.3 A due to the initial local linearity of the BH curve. For small signals, the magnetic field is low and does not reach the non-linear part, thus, the inductance is not dependent by the current. The third observation concerns the magnetic saturation of the steel. The inductance increases because the material can not manage all the magnetic field, and the induced current does not increase with the prescribed current. In Section 5.1, the freewheeling analysis for the load characterization will be described through a simulation with impulse response for the workpiece identification. Then, in Section 5.2, the PFM control is used to regulate the power during the heating operation mode with passing anisotropy. The resonant tank is designed to work at (6 A-max, 80 kHz), with a capacitor of 29 nF in series to a 0.5 Ω resistance. The current in the coil and the threshold limitations of the converter will be tracked on the RL maps of Figure 5 for a single grid waveform.

#### 5.1. Freewheeling Load Characterization

The load is characterized by its natural transient during the switching between phase I and phase II of the nominal working operation. Figure 6 represents the voltage over the capacitor for the geometry variation as anisotropy (left) and the temperature variation (right). The voltage starts from the maximum grid voltage. Then, when the IGBT is turned

off, the current in the inductor flows in the capacitor, reaching the breakdown voltage of the diode. Thus, the first lower crest is damped. In the left figure, the main effect of the anisotropy sliding is the decrease in the resistance and the increase in the inductance. Lower eddy currents inside the material result in higher magnetic field energy stored in the whole domain. In the right figure, the voltage resonance is compared for different temperatures. For low-temperature variation below the Curie temperature, it has no influence on the resonant frequency and has a soft impact on the damping resistance coefficient.

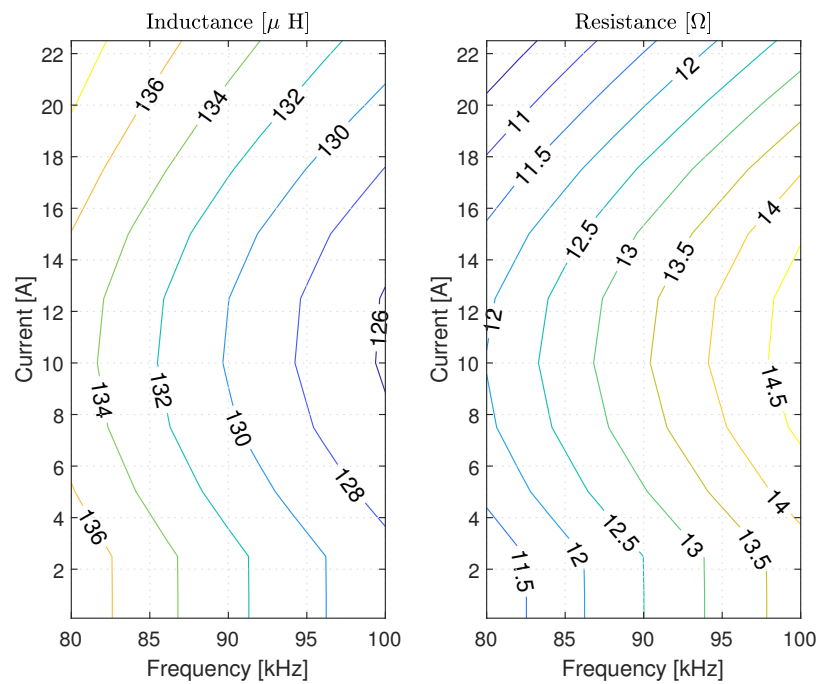


**Figure 5.** Maps of equivalent resistance and inductance for the load considered in Figure 1 in frequency–current interval of (80–100 kHz × 0.1–22.5 A) at room temperature. The data are sampled for each 2 kHz and 2.5 A, generating a 11 × 11 map. The optimal working point in the described range is found at (10 A, 100 kHz). The sweep parameter simulation was run on a 16Gb-RAM calculator @3.4 GHz. The average analysis calculation time for each couple of parameters is 15 min.

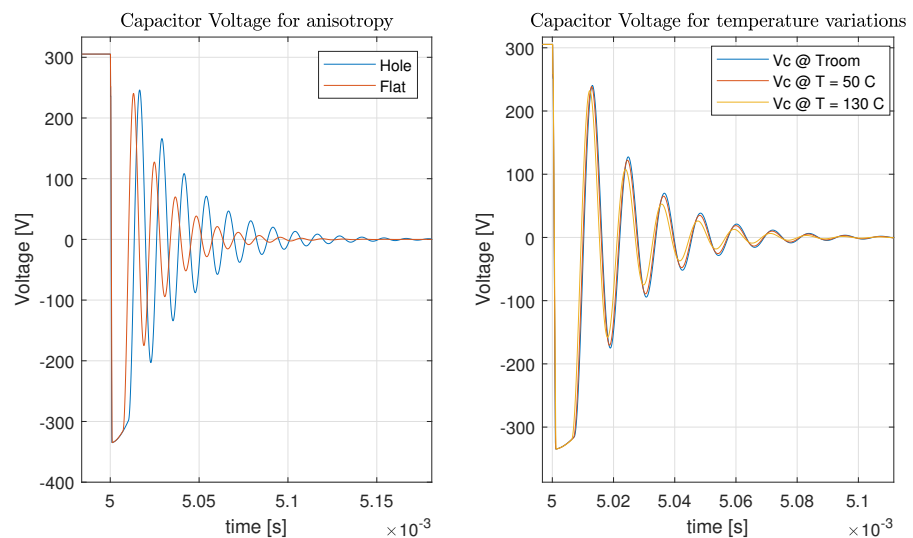


**Figure 6.** Natural time transient of capacitor voltage for the standard workpiece and for anisotropy presence (left) and capacitor voltage for different average temperatures of the workpiece surface (right).

### 5.2. Heating Operating Mode

In the heating operating mode, the inverter supplies the resonant tank with the grid voltage waveform. Thus, the high frequency current will be modulated with a 50 Hz grid carrier. The PFM control is initialized with a soft-start with constant frequency at 80 kHz. After an half period of the grid waveform the PFM control is enabled to reach the power reference. The Figure 7 represents the switching control, the current in the diode, the current the coil and the collector-emitter voltage. The represented quantities are taken from the maximum inductor current instant during the heating simulation of the workpiece without anisotropies. The IGBT currents are the overlapping of the discharge diode currents during the switching and the transistor currents during the I phase. The discharge currents in the diode match the collector voltage drop.

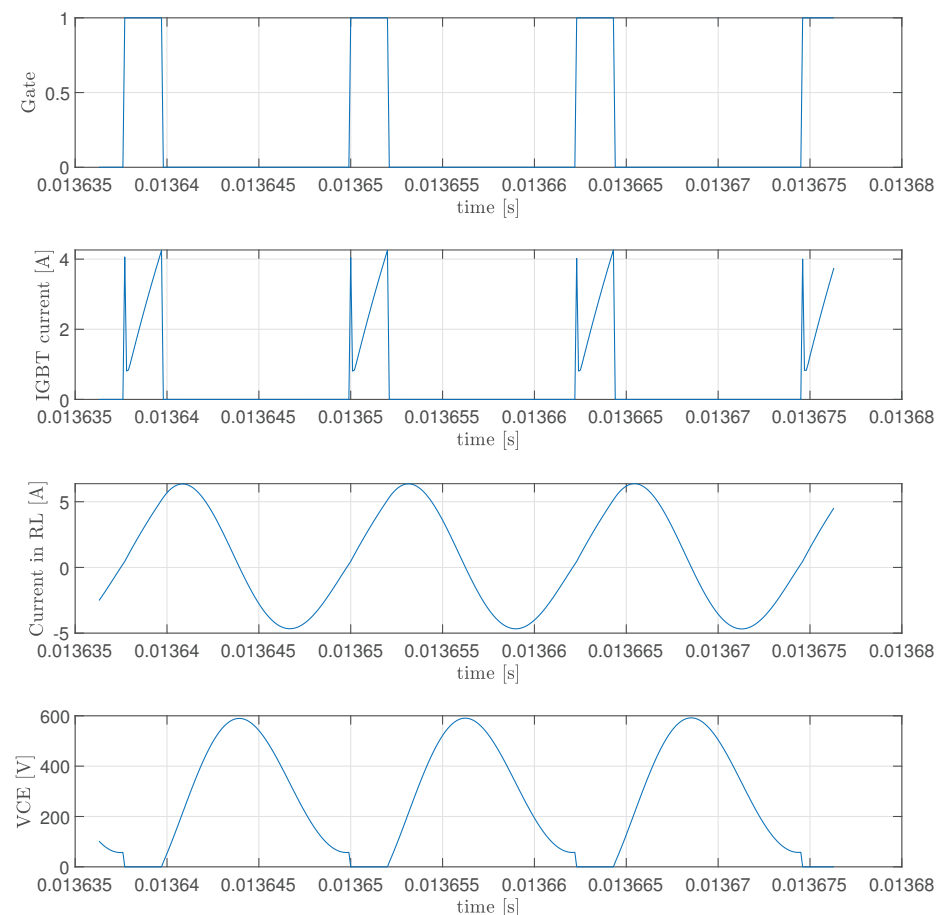


**Figure 7.** In order: IGBT gate control signal, flowing current in IGBT, current in the inductor and collector–emitter voltage drop on the IG resistance plots in the instant in which the maximum current flows in the inductor with nominal surface heating.

A better view of the grid carrier harmonic is represented in the bottom pictures in the Figure 8. Here is represented the comparison between the current amplitude without anisotropy and with the anisotropy. In order to follow the reference power, the maximum current must increase to compensate a lower equivalent resistance. The first two plots of Figure 8 represent the time-domain equivalent parameters output from the look-up tables for the two operative situations. Both are compared to fixed impedance values measured at low current at the operation frequency. In the Table 2, the results of time-dependent impedance are compared to results with fixed impedance. The variation of the resistance due to the grid waveform is the 5% of the nominal value. With the introduction of the anisotropy in the heating zone the resistance drops by 22%.

**Table 2.** Comparison between resulting quantities obtained with fixed impedance and waveform dependent impedance.

Compared Quantity	Difference
Maximum generated power during transient	10.1 W
Maximum coil current at power regulation equilibrium	0.27 A
Maximum collector voltage at power regulation equilibrium	13.1 V
Maximum resistance	0.56 Ω
Maximum inductance	1.32 μH

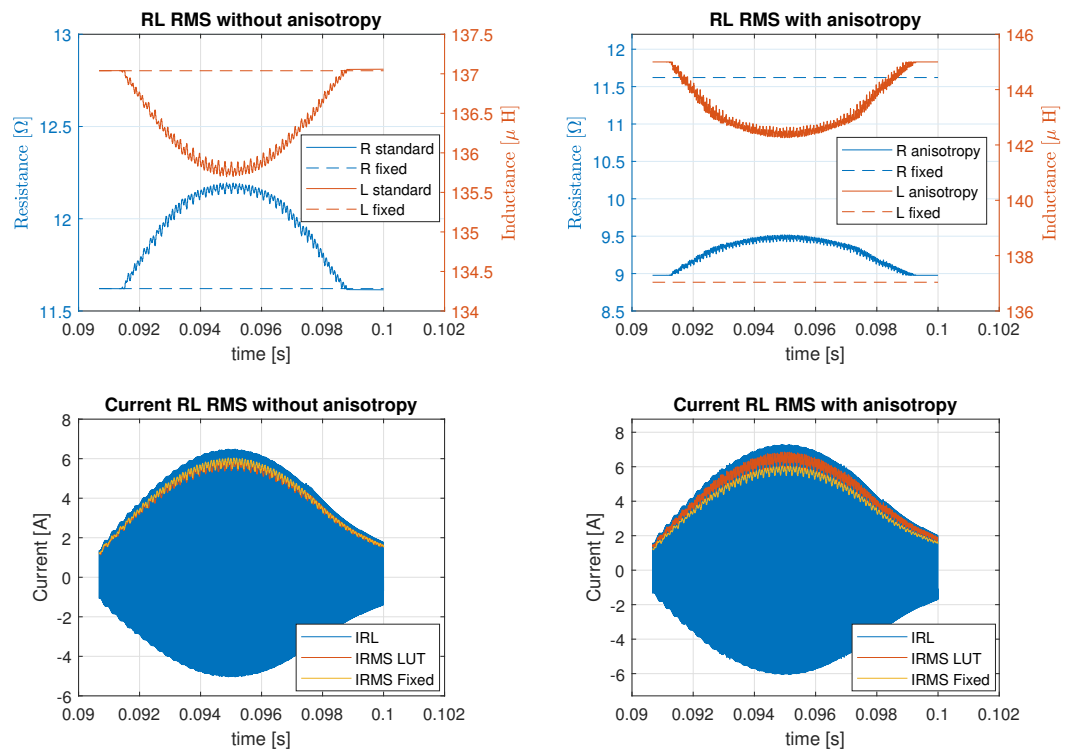


**Figure 8.** Equivalent rms R–L parameters during an half grid waveform carrier. The variation of the current and frequency in the control horizon generates a variation in the equivalent parameters.

Some considerations can be drawn from a larger temporal scale: in Figure 9 the power reference and the generated power are represented in the whole simulation time. The controlled quantity, the turn-on time, is represented in the second plot. With the occurrence of the anisotropy, in order to ensure the power reference, the turn-on time is regulated to reach higher currents. Finally, the observed frequency is represented in the third plot. It falls down with the increase in the inductance, according to Equation (10).

$$f_{res} = \frac{1}{2\pi} \sqrt{\frac{1}{L(f, I_{RL}, T(t), t)C_{res}} - \frac{R(f, I_{RL}, T(t), t)^2}{4L(f, I_{RL}, T(t), t)^2}} \tag{10}$$

An informative result to analyze the compatibility of the coil-workpiece system with the converter is represented in Figure 10. The equivalent RL parameters out of the look-up tables during the half-grid period are plotted (black dots) on the RL map along with the constraints described in Section 3.5. The main constraint that limits the feasibility of the operative working conditions is the maximum collector–emitter voltage. Two common limits for commercial IGBTs (600[V – AC] and 1200[V – AC]) are represented in red dashed lines. The lines are calculated according to Equation (6) with grid voltage. The figure is a very informative tool that can be used to assess that the designed IH system does not

exceed the safe operative thresholds, the coil-current amplitude, the frequency variation during the converter operation, and the RL variations for the grid waveform. Moreover, it offers a valid tool for the converter parameters tuning for the choice of the working frequency and the average power. The plot is useful to verify the IH system performance with the presence of the anisotropies and workpiece at different temperatures.

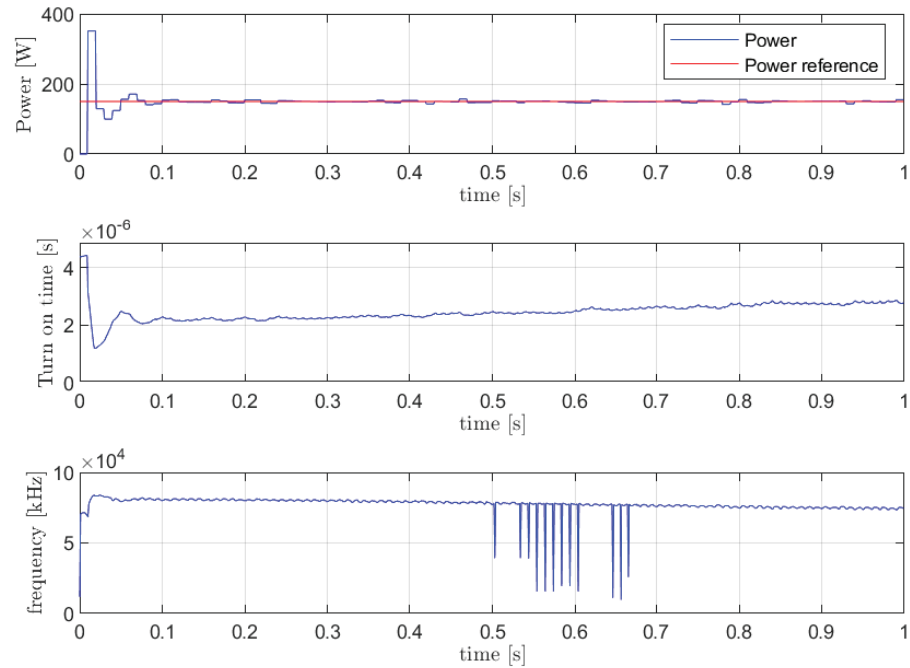


**Figure 9.** Power transient due to PFM control, turn-on time and estimated frequency in the control horizon during the anisotropy sliding ( $v_z = 3$  cm/s).

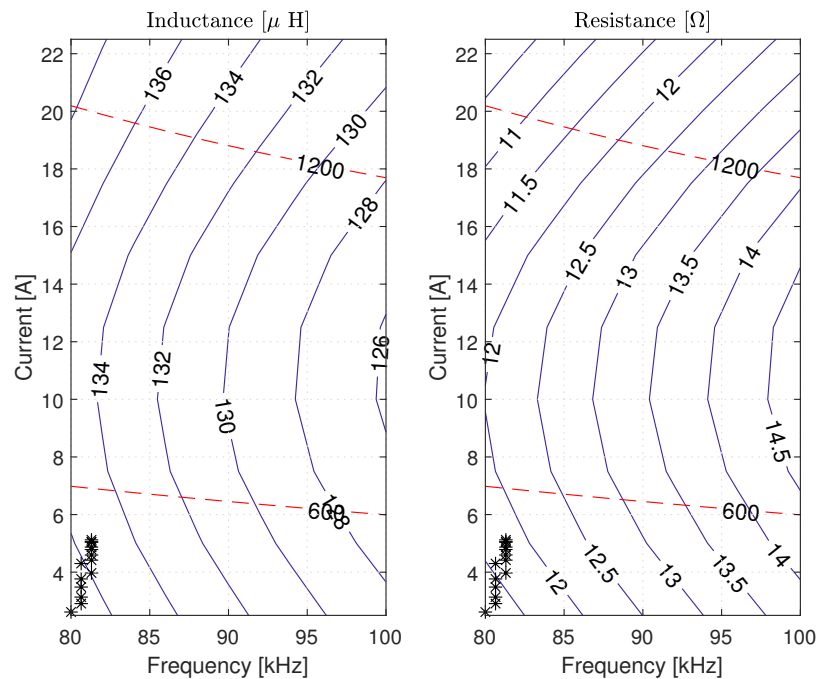


**Figure 10.** RL maps with safe operative limit constraints (red dotted lines) representing the maximum collector–emitter voltage on the diode and the operation area of the converter (black stars).

## 6. Conclusions

We have proposed a methodology to emulate the behavior of the load in induction heating applications through a lumped parameters circuitual representation. Using frequency stationary finite elements analysis, an emulation of the load is build to simulate the converter–load coupled system for different working conditions. The model allows to evaluate the dependency of the converter behavior on the temperature, current waveform, and the presence of anisotropies. The methodology is applied on a not-axi-symmetrical 3D case study, where time-domain transient FEA simulations are unfeasible. Moreover, the proposed approach allows to tune the converter parameters and to analyze the converter working region during the whole heating task.

A map that illustrates the variations of the impedance values and also the distance to the safe operative thresholds is proposed. This map is useful for the co-design process of the full induction heating system. It allows to track the converter behavior for long operation times, for example, during the passage of an anysotropy or the full heating task.

Possible extensions for future works are the experimental validation of the technique and its comparison with FEM time-domain simulations. Additionally, the usage of the surrogate models for extrapolation of RL equivalent parameters outside the operative map and the lumped representation of non-homogeneous temperature variations on the workpiece.

**Author Contributions:** Conceptualization, E.S., F.R. and G.G.; methodology, E.S., F.R. and G.G.; validation, E.S., F.R. and G.G.; formal analysis, E.S.; investigation, E.S., F.R. and G.G.; writing—original draft preparation, E.S., F.R. and G.G.; writing—review and editing, E.S., F.R. and G.G.; visualization, E.S., F.R. and G.G.; supervision, F.R. and G.G. All authors have read and agreed to the published version of the manuscript.

**Funding:** This research received no external funding.

**Data Availability Statement:** Not applicable.

**Conflicts of Interest:** The authors declare no conflict of interest.

## References

1. Lupi, S. *Fundamentals of Electroheat: Electrical Technologies for Process Heating*; Springer: Cham, Switzerland, 2017. [[CrossRef](#)]
2. Rapoport, E.; Pleshivtseva, Y. *Optimal Control of Induction Heating Processes*, 1st ed.; CRC Press: Boca Raton, FL, USA, 2006. [[CrossRef](#)]
3. Vishnuram, P.; Ramachandiran, G.; Ramasamy, S.; Dayalan, S. A comprehensive overview of power converter topologies for induction heating applications. *Int. Trans. Electr. Energy Syst.* **2020**, *30*, e12554, .: 10.1002/2050-7038.12554. [[CrossRef](#)]
4. Pisano, M.; Bizzarri, F.; Brambilla, A.; Gruosso, G.; Gajani, G.S. Micro-inverter for solar power generation. In Proceedings of the SPEEDAM 2012—21st International Symposium on Power Electronics, Electrical Drives, Automation and Motion, Sorrento, Italy, 20–22 June 2012; pp. 109–113. [[CrossRef](#)]
5. Pablo Ochoa Aviles, J.; Silva, V.V.R.; Tofoli, F.L. Household induction cooking system based on a grid-connected photovoltaic system. *IET Circuits Devices Syst.* **2020**, *14*, 1117–1128. [[CrossRef](#)]
6. Herasymenko, P.; Yurchenko, O. An Extended Pulse-Density-Modulated Series-Resonant Inverter for Induction Heating Applications. In Proceedings of the 2020 IEEE 61th International Scientific Conference on Power and Electrical Engineering of Riga Technical University (RTUCON), Riga, Latvia, 5–7 November 2020; pp. 1–8. [[CrossRef](#)]
7. Herasymenko, P. Study of the suitable value of dead-time between control signals of transistors for a series-resonant inverter with phase-shift control in induction heating systems. *EUREKA Phys. Eng.* **2021**, *3*, 60–70. [[CrossRef](#)]
8. Vishnuram, P.; Ramachandiran, G.; Sudhakar Babu, T.; Nastasi, B. Induction Heating in Domestic Cooking and Industrial Melting Applications: A Systematic Review on Modelling, Converter Topologies and Control Schemes. *Energies* **2021**, *14*, 6634. [[CrossRef](#)]
9. Ozturk, M.; Aslan, S.; Altintas, N.; Sinirlioglu, S. Comparison of Induction Cooker Power Converters. In Proceedings of the 2018 6th International Conference on Control Engineering and Information Technology (CEIT), Istanbul, Turkey, 25–27 October 2018; pp. 1–6. [[CrossRef](#)]
10. Züngör, F.; Emre, B.; Öz, B.; Öztürk, M. A New Load Detection Method and Circuit Analysis for Quasi Resonant Inverter. In Proceedings of the 2021 10th International Conference on Renewable Energy Research and Application (ICRERA), Istanbul, Turkey, 18–21 September 2022; pp. 40–46. [[CrossRef](#)]
11. Li, Z.F.; Hu, J.C.; Huang, M.S.; Lin, Y.L.; Lin, C.W.; Meng, Y.M. Load Estimation for Induction Heating Cookers Based on Series RLC Natural Resonant Current. *Energies* **2022**, *15*, 1294. [[CrossRef](#)]

12. Ozturk, M.; Zungor, F.; Emre, B.; Oz, B. Quasi Resonant Inverter Load Recognition Method. *IEEE Access* **2022**, *10*, 89376–89386. [[CrossRef](#)]
13. Sarnago, H.; Lucia, O.; Burdio, J.M. High-Performance Class-E Quasi-Resonant Inverter for Domestic Induction Heating Applications. In Proceedings of the 2022 IEEE Applied Power Electronics Conference and Exposition (APEC), Houston, TX, USA, 20–24 March 2022; pp. 1202–1207. [[CrossRef](#)]
14. COMSOL AB. COMSOL Multiphysics. Available online: <https://doc.comsol.com/5.4/doc/com.comsol.help.acdc/ACDCModuleUsersGuide.pdf> (accessed on 24 January 2023).
15. Boadi, A.; Tsuchida, Y.; Todaka, T.; Enokizono, M. Designing of suitable construction of high-frequency induction heating coil by using finite-element method. *IEEE Trans. Magn.* **2005**, *41*, 4048–4050. [[CrossRef](#)]
16. Pascual, A.; Acero, J.; Burdío, J.; Carretero, C.; Llorente, S. Electrothermal analysis of temperature-limited loads for domestic induction heating applications. In Proceedings of the IECON 2022—48th Annual Conference of the IEEE Industrial Electronics Society, Brussels, Belgium, 17–20 October 2022; pp. 1–6. [[CrossRef](#)]
17. Martín-Segura, G.; Ferrater-Simon, C.; Lopez-Mestre, J.; Montesinos-Miracle, D.; Bergas-Jane, J. Simulation of an induction hardening system during Curie temperature transition considering converter’s performance. *COMPEL Int. J. Comput. Math. Electr. Electron. Eng.* **2013**, *32*. [[CrossRef](#)]
18. Kovac, D.; Melnykov, V. Simulation and Laboratory Model of Induction Heating in COMSOL Multiphysics. In Proceedings of the 2021 IEEE International Conference on Modern Electrical and Energy Systems (MEES), Kremenchuk, Ukraine, 21–24 September 2021; pp. 1–6. [[CrossRef](#)]
19. Martín Segura, G. Induction Heating Converter’s Design, Control and Modeling Applied to Continuous Wire Heating. Ph.D. Thesis, Departament d’Enginyeria Elèctrica, Universitat Politècnica de Catalunya, Barcelona, Spain, 2012.
20. Kagimoto, H.; Miyagi, D.; Takahashi, N.; Uchida, N.; Kawanaka, K. Effect of Temperature Dependence of Magnetic Properties on Heating Characteristics of Induction Heater. *IEEE Trans. Magn.* **2010**, *46*, 3018–3021. [[CrossRef](#)]
21. Takau, L.; Bodger, P. Low frequency modelling of induction heaters using series equivalent circuit, transformer equivalent circuit and finite element analysis. In Proceedings of the 2013 Australasian Universities Power Engineering Conference (AUPEC), Hobart, TAS, Australia, 29 September–3 October 2013; pp. 1–6. [[CrossRef](#)]
22. Aguilar-Peréz, L.A.; Merino-García, J.A.; Ramírez-Crescencio, F.; Villanueva-Fierro, I.; Torres-SanMiguel, C.R. Experimental design and numerical validation of a low-cost water heater by electromagnetic induction. *Adv. Mech. Eng.* **2021**, *13*, 16878140211055251.
23. Giuffrida, C.; Gruosso, G.; Repetto, M. Finite formulation of nonlinear magnetostatics with integral boundary conditions. *IEEE Trans. Magn.* **2006**, *42*, 1503–1511. [[CrossRef](#)]
24. Khazaal, M.H.; Abdulbaqi, I.M.; Thejel, R.H. Modeling, design and analysis of an induction heating coil for brazing process using FEM. In Proceedings of the 2016 Al-Sadeq International Conference on Multidisciplinary in IT and Communication Science and Applications (AIC-MITCSA), Baghdad, Iraq, 9–10 May 2016; pp. 1–6. [[CrossRef](#)]
25. Powersimtech. PSIM. Available online: <https://powersimtech.com/> (accessed on 24 January 2023).

**Disclaimer/Publisher’s Note:** The statements, opinions and data contained in all publications are solely those of the individual author(s) and contributor(s) and not of MDPI and/or the editor(s). MDPI and/or the editor(s) disclaim responsibility for any injury to people or property resulting from any ideas, methods, instructions or products referred to in the content.